

# Modelling flow across the aortic valve using finite elements and static Navier Stokes

Cesare Magnetti

King's College London, London WC2R 2LS, UK.  
School of Biomedical Engineering and Imaging Sciences  
<https://www.kcl.ac.uk/bmeis>

**Abstract.** Aortic Stenosis is the most common heart valvular disease and affects roughly 2% of the elderly population. Treatment of severe cases involves surgical replacement of the Aortic Tricuspid Valve with prosthetic ones, which often lead to complications due to unaccounted blood flow through the valve. To ensure correct blood flow, such prosthetic valves must be meticulously designed, this is done through computational flow simulations to gain insights on the velocity and pressure distributions through the aortic valve along with the stresses they produce on the artificial leaflets. To this end, a FEM routine was developed to solve a static, incompressible-flow simplification of Navier Stokes' equations coupled with Continuity equation, approximating the pressure and velocity fields throughout an idealized, axisymmetric 2D projection of the aortic sinus and downstream Aorta. The number of assumptions taken through this paper are excessively large to have any clinical purpose and the scope of this work is merely to analyze the computational approach adopted to solve such problems and its accuracy.

**Keywords:** Finite Element Method · Aortic Stenosis · Aortic Valve Flow

## 1 Introduction

The following paper proposes a Finite Element Method (FEM) analysis to evaluate the pressure drop between the inlet and outlet boundaries of the Aortic Valve. This is achieved solving a static, incompressible flow Stokes problem during Peak Flow, where the change in momentum is zero. We model the Aortic Valve and Downstream Aorta using four increasingly dense triangular meshes (see fig.1) where the domain is assumed to be rigid. The pressure and velocity fields will be calculated solving Navier Stokes coupled with Continuity Equation and will be used to determine the pressure drop through

the valve, which will be compared to results obtained by [14] as an indicator of accuracy.

Aortic Stenosis (AS) is a restriction of the outflow area of the left ventricle of the heart, which usually occurs at the level of the Aortic (Tricuspid) Valve [2], preventing it to open properly. Causes of such narrowing can be a congenital Aortic Bicuspid Valve, a scarred Aortic Valve due to Rheumatic Fever or the wearing of the valve in the elderly population. Furthermore, AS can be caused by an excessive deposit of calcified materials on the leaflets of the aortic valve, leading to a thickening of the tissues [1]. It follows that more pressure is needed to drive the blood through the Aortic Valve, forcing the heart to work more than necessary, which can lead to serious injuries. Typical symptoms of severe cases include loss of consciousness, chest pain, shortness of breath (with or without activity) and swollen legs and feet. About 2% of the elderly population ( $> 65\text{ years old}$ ) is affected by AS and the chances of death in five and ten years if not treated are respectively of 50% and 90% [2]. The main treatment procedure involves valve replacement surgery with artificial leaflets structures [3, 4].

The adopted routine is important to analyse Aortic Stenosis (AS) effects on the blood flow through the aortic sinus and to model artificial leaflets structures for surgical implants. To this end FEM routines can be used to test the performance of the artificial valves under simulated blood flows, identifying the strengths and weaknesses of the prosthetic valve under inspection. Note that, as explained in sec.3.2, this paper makes several assumptions, including approximating blood to be a Newtonian fluid using Navier Stokes to model the problem. On the other hand, research has shown that blood viscosity is a function of the shear rate [9, 10], making it Non-Newtonian in nature. For these reasons the achieved results do not have enough ground to be used for any clinical purpose and are merely an investigation of the FEM routine needed to solve such problems and its accuracy.

## 2 Literature Review

The most similar piece of work, to the best of our knowledge, to the one proposed in this paper can be found at [14]. In their work, the authors propose a finite element analysis to solve a steady laminar flow Navier Stokes problem, through a 2D projection of the aortic sinus and downstream Aorta. Furthermore, they compare flow and pressure distributions, along with the stress field, through three different prosthetic valves to assess their performance.

Similarly to our work, they assumed blood to be a Newtonian incompressible homogeneous fluid flowing through a rigid, axisymmetric domain at peak flow, where the rate of change of the velocity drops to zero. Our work further assumes uniform inlet/outlet flows at boundaries  $\Gamma_1, \Gamma_3$  (see fig.1). In particular, the boundary conditions proposed by the authors are identical to the ones used in this paper with the exception of a laminar inflow defined as  $\vec{v}_0(x_2) = [v_0(1 - \frac{|x_2|^2}{\max(x_2)^2}), 0]^T \forall x_2 \in \Gamma_1$  rather than the uniform inflow  $\vec{v}_0 = (-200, 0)^T \forall x_2 \in \Gamma_1$  reported in eq.7. Furthermore, they enforced natural boundary conditions to the prosthetic valves being initially at rest, but lacked to consider coronary outlets; note that such prosthetic valves are directly integrated in the domain mesh.

The authors used Newton-Raphson iterative method to solve Navier Stokes coupled with Continuity equations in a similar manner as described in sec.3.4, however they used adaptively refined quadrilateral elements to discretise the domain rather than the triangular meshes shown in fig.1. Quadratic interpolators  $\hat{\phi}$  were used to approximate the velocity and linear interpolators  $\hat{\psi}$  for the pressure, since this procedure was also conducted in this paper, refer to sec.3.1 for more details about on the topic. On another note, the authors additionally proposed flow simulations for different Reynold numbers, defined as  $Re = \frac{VD\rho}{\mu}$ , where D is the diameter of the vessel at the level of aortic valve, V is the average velocity at D and  $\mu$  and  $\rho$  are respectively the viscosity and density of the fluid. Higher Reynold numbers were achieved iteratively increasing the fluid density  $\rho$  and using the current solution as an initial guess for Newton Raphson for the next Reynold number simulation, in a similar manner as the

dampening experiment described in sec.4.1. Theoretically, for higher Reynold numbers the turbulence in the flow should increase, whereas low Reynold numbers are characterised by a coherent laminar flow.

Their results show monotonically increasing pressure drops ranging in [0.02  $KPa$ , 0.185  $KPa$ ] for Reynold numbers in [10, 2000]<sup>1</sup>, along with insightful velocity and stress distribution plots showing the effectiveness of each prosthetic valve under inspection and their potential problems, such us thrombus formation or blockage of the valve. These values will be used as a ground truth to assess the accuracy achieved by the simplified approach used in this paper; note that Reynold numbers are not meaningful under the uniform inflow assumption taken through this work, therefore the comparison is not strict. On the other hand a large bias from the above results may be an indicator that the achieved solution is not accurate, meaning that modelling errors and/or simulation errors are excessively large.

### 3 Methods

A FEM routine was developed to evaluate the velocity and pressure distributions over the domain solving a static flow simplification of Navier Stokes' equations coupled with continuity equation. Additionally, the pressure drop between the inlet and outlet boundaries of the domain will be evaluated using two different procedures and the variance of the the achieved results will be used as an additional indicator of accuracy.

#### 3.1 Problem Domain Setup

Four increasingly dense 2D meshes (fig.1) will be utilised to approximate the aortic sinus and downstream aorta. Each mesh consists of local triangular elements which are more dense in proximity of the aortic valve and coronary arteries.

---

<sup>1</sup> Reynold numbers are dimentionless quantities.

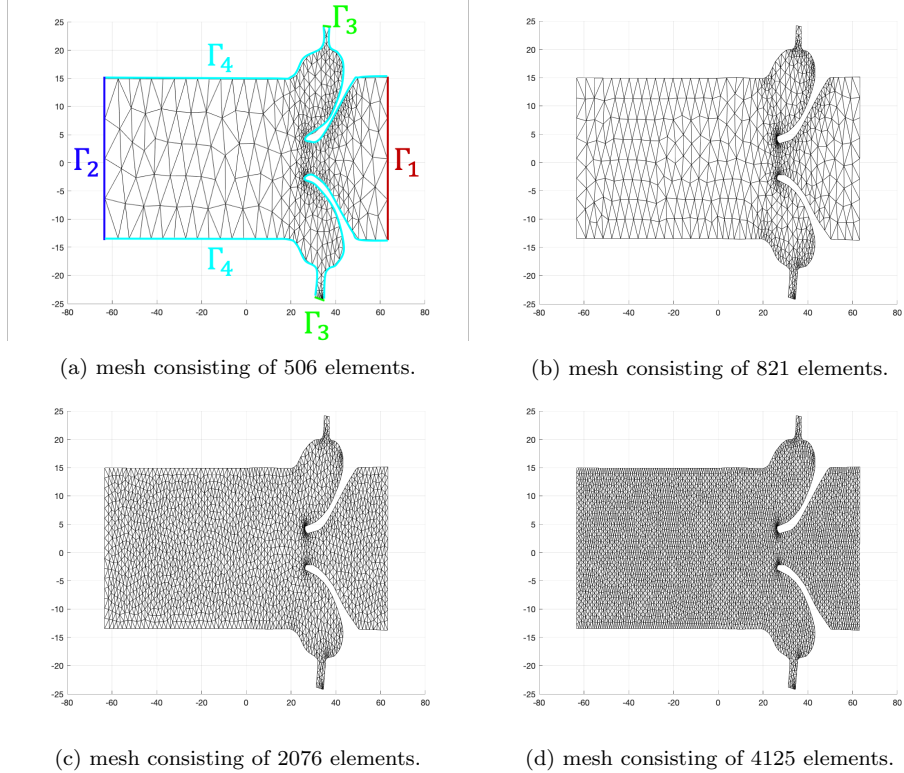


Fig. 1: Diagram depicting the four meshes utilised throughout this problem. Note that the triangular elements are more densely distributed near the aortic valve, which is the region of interest of the problem. The vertical and horizontal axes in each diagram represent respectively the  $x_2$  (axial plane) and  $x_1$  (transverse plane) coordinates and the inlet and outlet boundaries are respectively labelled with  $\Gamma_1$  and  $\Gamma_2$  in sub-figure (a). The coronary outlets are then labelled using  $\Gamma_3$  and the aortic sinus and downstream aorta walls are labelled using  $\Gamma_4$ . As it will be explained, we have inflow and outflow Dirichlet boundary conditions on  $\Gamma_1$  and  $\Gamma_3$  and a Neumann natural condition on  $\Gamma_2$ . All nodes on  $\Gamma_4$  will be enforced to have a *no slip condition* on the velocity components.

During the finite element routine, local elements  $e_k$  will be mapped to a normalized triangular master element  $e_m$  through a linear mapping  $\vec{p}_k : e_k \Rightarrow e_m, \vec{p}_k(\xi_1, \xi_2) = (x_1, x_2)^T$ . This step is needed in order to integrate over triangular elements using *Gaussian quadrature*. There are many choices of mappings, fig.2 reports the procedure using *Nodal Shape Functions* for a detailed explanation of such procedure please refer to [16, 17].

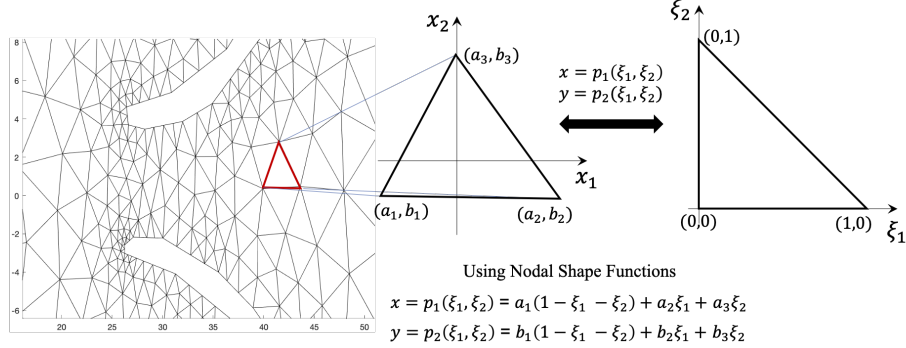


Fig. 2: Diagram showing the mapping from a local element of the mesh to the triangular master element  $e_m$  using Nodal Shape Functions. In the case of triangular elements the three nodal shape functions are defined as  $N_1 = (1 - \xi_1 - \xi_2)$ ,  $N_2 = \xi_1$  and  $N_3 = \xi_2$ . Mapping  $\vec{p}_k(\xi_1, \xi_2)$  is then exploited to map the master element on top of the local element (or vice versa).

A continuous quadratic approximation-space  $\mathbf{P}_2$  will be used to infer blood velocity and a continuous linear approximation-space  $\mathbf{P}_1$  for the blood pressure. It follows that the true solutions  $\vec{v}$  and  $p$  will be approximated by discrete formulations  $\vec{v}^h$  and  $p^h$ , which will be expressed as a weighted sum of Lagrangian basis functions  $f = \sum_i f_i \hat{\phi}_i(x_1, x_2) \Leftrightarrow \sum_i f_i \phi_i(\xi_1, \xi_2)$  in local and master element coordinates. Lagrangian interpolators for the velocity  $\hat{\phi}_i$  will have quadratic nature and for the pressure  $\hat{\psi}_i$  will be linear. Hence the finite, discrete approximations of  $\vec{v}$  and  $p$  are mathematically formulated as:

$$\begin{cases} \vec{v}^h = \sum_i^N \sum_j^K v_i^j \mathbf{e}_j \hat{\phi}_i(x_1, x_2) \Leftrightarrow \sum_i^N \sum_j^K v_i^j \mathbf{e}_j \phi_i(\xi_1, \xi_2) \\ p^h = \sum_i^M p_i \hat{\psi}_i(x_1, x_2) \Leftrightarrow \sum_i^M p_i \psi_i(\xi_1, \xi_2) \end{cases} \quad (1)$$

where  $N, M$  and  $K$  are respectively the number of nodes for the velocity and pressure and the number of components of the velocity (in this problem  $K = 2$ ).

Note that the choice of approximating the pressure with a lower interpolation order is a commonly accepted procedure to satisfy the

*inf-sup* condition; using a  $\mathbf{P}_2$  approximation space on the pressure can yield to the inversion of a singular matrix and unstable convergence. In particular this will imply a discontinuous distribution of the pressure with significant outliers in between nodes. For more information on the above statements please refer to [18, 19]. Finally, the change of coordinates on integral quantities can be simply performed multiplying by the determinant of the Jacobian tensor, a two point tensor containing the partial derivatives of a reference frame with respect to the other.

$$\int_{\Omega} R(x_1, x_2) dx_1 dx_2 \Leftrightarrow \int_{e_m} R(x_1(\xi_1, \xi_2), x_2(\xi_1, \xi_2)) \det(J) d\xi_1 d\xi_2$$

$$\text{where } J = \begin{bmatrix} \frac{\partial x_1}{\partial \xi_1} & \frac{\partial x_2}{\partial \xi_1} \\ \frac{\partial x_1}{\partial \xi_2} & \frac{\partial x_2}{\partial \xi_2} \end{bmatrix} \quad (2)$$

### 3.2 Strong Form Derivation

The first step taken in order to define the strong form of the problem was to simplify Navier Stokes' equations through the following assumptions:

- *Peak Flow instant*: throughout this problem we will only consider the peak flow instant, where the aortic valve leaflets are in their maximally dilated positions and the instantaneous rate of change in momentum drops to zero. This will in turn simplify all partial derivatives of the velocity with respect to time.
- *No External Body Forces*: blood is affected both by gravitational force and by the electromagnetic force generated from the heart itself [8]. Both will be discarded throughout this project.
- *homogeneous viscosity and pressure fields*: throughout this project blood will be treated as an incompressible fluid flowing through a rigid body approximation of the aortic sinus and downstream aorta, which are in fact hyper elastic in nature. That is, blood density  $\rho = 1e - 03 g mm^{-3}$  is assumed to be constant throughout a static, rigid domain. Furthermore, the Newtonian assumption of blood flow allows us to take yet another approximation considering its viscosity  $\mu = \frac{\text{shear stress}}{\text{strain rate}} = 4e - 02 g(mms)^{-1}$  to be constant [11].
- *constant inflow/outflow boundary conditions*: blood inflow at the left ventricle boundary  $\Gamma_1$  and outflow at the coronary sinus  $\Gamma_3$

will be approximated to be uniformly distributed throughout the boundaries.

The strong form derivation then develops starting from Navier Stokes:

$$\rho \frac{D\vec{v}}{Dt} = -\nabla p + \rho \vec{g} + \mu \nabla \cdot \nabla \vec{v} \quad (3)$$

where  $\frac{D\vec{v}}{Dt} = \frac{\partial \vec{v}}{\partial t} + \vec{v} \cdot \nabla \vec{v}$  is the material derivative of the blood velocity formed by its partial derivative respect to time plus the vorticity component. A full derivation of Navier Stokes' Equations is beyond the scope of this paper and can be found at [12]. Acknowledging the *Peak Flow instant* assumption the partial derivative of velocity with respect to time drops to zero, furthermore since we are not considering external body forces,  $\vec{g}$  simplifies in eq.3 leading to the following equation:

$$\rho \vec{v} \cdot \nabla \vec{v} - \mu \nabla \cdot \nabla \vec{v} + \nabla p = 0 \quad (4)$$

The continuity equation for an incompressible fluid can be derived from Reynold's Transport Theorem [13] and conservation of mass to be:

$$\frac{\partial \rho}{\partial t} + \nabla \cdot (\rho \vec{v}) = 0 \quad (5)$$

A full derivation of the above equation can be found at [15]. Recalling that we are under the assumption of constant density in a static, rigid domain, the equation can be further simplified to:

$$\nabla \cdot \vec{v} = 0 \quad (6)$$

This will in turn lead to the definition of the strong form of the problem as:

$$\begin{cases} \rho \vec{v} \cdot \nabla \vec{v} - \mu \nabla \cdot \nabla \vec{v} + \nabla p = 0, & \text{on } \Omega \\ \nabla \cdot \vec{v} = 0 & \text{on } \Omega \\ \vec{v} = \vec{v}_0 = (-200, 0)^T \text{ mm s}^{-1} & \text{on } \Gamma_1 \\ \mu \nabla \vec{v} - p \mathbf{I} = 0 & \text{on } \Gamma_2 \\ \vec{v} = \vec{v}_1 = \begin{cases} (0, 10)^T & \text{if } x_2 > 0 \\ (0, -10)^T & \text{if } x_2 < 0 \end{cases} & \text{on } \Gamma_3 \\ \vec{v} = 0 & \text{on } \Gamma_4 \end{cases} \quad (7)$$

where  $\Omega$  and  $\Gamma_{1-4}$  indicate respectively the problem domain and the different boundaries (see fig.1). Note that a constant Dirichlet inflow condition is applied at  $\Gamma_1$  and a constant Dirichlet outflow condition on  $\Gamma_3$ . No-slip condition will be applied on the walls of the aortic sinus and downstream aorta ( $\Gamma_4$ ), setting the velocity to zero. Finally, a natural Neumann condition on the known boundary flux on  $\Gamma_2$  is given to be zero.

### 3.3 Weak Formulation

The system is currently satisfied by infinite solutions, in order to find the best approximation, we must enforce orthogonality of the solution to any possible function lying in the solution space. In many dimensions this is achieved by an inner product between the solution and test function equal to zero; that is integrating over the problem domain  $\Omega$  and multiplying by test functions as follows:

$$\begin{cases} \int_{\Omega} \rho \vec{v} \cdot \nabla \vec{v} \cdot \vec{w} - \mu \nabla \cdot \nabla \vec{v} \cdot \vec{w} + \nabla p \vec{w} \cdot \partial \Omega = 0 \\ \int_{\Omega} \nabla \cdot \vec{v} g \cdot \partial \Omega = 0 \end{cases} \quad (8)$$

where  $\vec{w}$  and  $g$  are respectively a vector of test functions for the velocity and a scalar test function for the pressure, they represent any possible function lying in their solution spaces, the above equations enforce  $\vec{v}$  and  $p$  to be orthogonal to such test functions. We will now use vector calculus identities to simplify the above equations:

$$\begin{aligned} \mu \nabla \cdot (\vec{w} \nabla \vec{v}) &= \mu \nabla \cdot \nabla \vec{v} \cdot \vec{w} + \mu \nabla \vec{v} : \nabla \vec{w} \\ \nabla \cdot (p \vec{w}) &= \nabla p \cdot \vec{w} + p \nabla \cdot \vec{w} \end{aligned} \quad (9)$$

both equations are a multidimensional generalisation of chain rule for the divergence operator; the first equation will be used to substitute the  $\mu \nabla \cdot \nabla \vec{v} \cdot \vec{w}$  term in eq.8 (top) and the second equation will substitute  $\nabla p \vec{w}$  in the same equation. Re-arranging yields to:

$$\begin{cases} \int_{\Omega} -\mu \nabla \cdot (\vec{w} \nabla \vec{v}) + \nabla \cdot (p \vec{w}) + \rho \vec{v} \cdot \nabla \vec{v} \cdot \vec{w} + \mu \nabla \vec{v} : \nabla \vec{w} - p \nabla \cdot \vec{w} \cdot \partial \Omega = 0 \\ \int_{\Omega} \nabla \cdot \vec{v} g \cdot \partial \Omega = 0 \end{cases} \quad (10)$$

Note that the first two terms in the above equation can be grouped together through the additive property of the divergence operator, then applying the divergence theorem:

$$\begin{cases} \int_{\Gamma} \vec{w}(-\mu \nabla \vec{v} + p \mathbf{I}) \cdot \hat{n} \partial \Gamma + \int_{\Omega} \rho \vec{v} \cdot \nabla \vec{v} \cdot \vec{w} + \mu \nabla \vec{v} : \nabla \vec{w} - p \nabla \cdot \vec{w} \partial \Omega = 0 \\ \int_{\Omega} \nabla \cdot \vec{v} g \partial \Omega = 0 \end{cases} \quad (11)$$

It is now possible to decompose the boundary integral between each boundary as:

$$\begin{aligned} \int_{\Gamma} \vec{w}(-\mu \nabla \vec{v} + p \mathbf{I}) \cdot \hat{n} \partial \Gamma &= \int_{\Gamma_1} \vec{w}(-\mu \nabla \vec{v} + p \mathbf{I}) \cdot \hat{n} \partial \Gamma_1 + \\ &\quad \int_{\Gamma_2} \vec{w}(-\mu \nabla \vec{v} + p \mathbf{I}) \cdot \hat{n} \partial \Gamma_2 + \int_{\Gamma_3} \vec{w}(-\mu \nabla \vec{v} + p \mathbf{I}) \cdot \hat{n} \partial \Gamma_3 \\ &\quad + \int_{\Gamma_4} \vec{w}(-\mu \nabla \vec{v} + p \mathbf{I}) \cdot \hat{n} \partial \Gamma_4 \end{aligned} \quad (12)$$

All above terms drop to zero as we have three Dirichlet conditions and the Neumann condition on  $\Gamma_2$  sets the integrand to zero. For more information about weak-form formulation and boundary integration see [20]. The *residual vectors* of the problem are then defined as:

$$\begin{cases} R_1 = \int_{\Omega} \rho \vec{v} \cdot \nabla \vec{v} \cdot \vec{w} + \mu \nabla \vec{v} : \nabla \vec{w} - p \nabla \cdot \vec{w} \partial \Omega = 0 \\ R_2 = \int_{\Omega} \nabla \cdot \vec{v} g \partial \Omega = 0 \end{cases} \quad (13)$$

We then proceed to discretise the domain  $\Omega$  and the solutions  $\vec{v}$  and  $p$  as explained in sec.3.1 to obtain the discrete formulation of the residual vectors.

$$\begin{cases} R_1^h = \int_{\Omega} \rho \vec{v}^h \cdot \nabla \vec{v}^h \cdot \vec{w}^h + \mu \nabla \vec{v}^h : \nabla \vec{w}^h - p^h \nabla \cdot \vec{w}^h \partial \Omega = 0 \\ R_2^h = \int_{\Omega} \nabla \cdot \vec{v}^h g^h \partial \Omega = 0 \end{cases} \quad (14)$$

Where all functions can be expressed as a weighted sum of Lagrangian basis functions  $f = \sum_i f_i \phi_i(x_1, x_2) \Leftrightarrow \sum_i f_i \phi_i(\xi_1, \xi_2)$  in

local and master element coordinates (see sec.3.1). The corresponding discrete solution and test spaces are defined as follows:

$$\begin{cases} \vec{v}^h \in \mathbb{V}^h := \{\vec{f} \in H^1(\Omega) | \vec{f}(\Gamma_1) = \vec{v}_0 \wedge \vec{f}(\Gamma_3) = \vec{v}_1 \wedge \vec{f}(\Gamma_3) = 0\} \\ \vec{w}^h \in \mathbb{V}_0^h := \{\vec{f} \in H^1(\Omega) | \vec{f}(\Gamma/\Gamma_2) = 0\} \\ p^h \in \mathbb{P}^h := \{f \in L^2(\Omega)\} \\ g^h \in \mathbb{P}_0^h := \{f \in L^2(\Omega)\} \end{cases} \quad (15)$$

### 3.4 Solve the System

To solve this non-linear system we must adopt an iterative approach, in this case *Newton-Raphson* [21] was chosen, a diagram explaining the algorithm is given in fig.3.

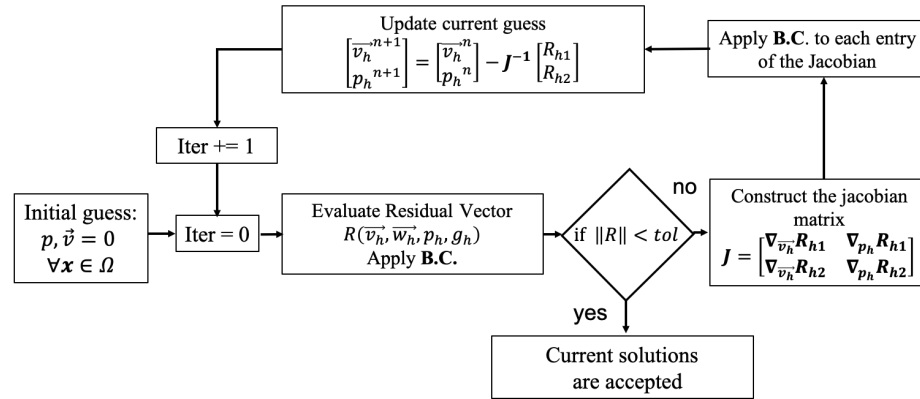


Fig. 3: Diagram depicting the basic implementation of Newton-Raphson's algorithm adapted to the problem of choice. We start with an initial guess of zero for  $\vec{v}$  and  $p$  and evaluate the current residual  $R^h = [R_1^h, R_2^h]^T$ , applying the boundary conditions to the boundary nodes of the residual. if the residual is below a certain tolerance ( $1e-06$  was chosen) then the solutions are accepted, otherwise we proceed to update the current guess through a multidimensional generalisation of Taylor Expansion and repeat the previous steps until convergence.

The Jacobian matrix  $J$  stems from the multidimensional generalisation of Taylor's Expansion, starting from a scalar 1D function:  $f(x + h) = f(x) + hf'(x) + O(h^2)$  where we seek for the solution  $x$  for which  $f(x) = 0$ . We can then rewrite  $0 = f(x) + hf'(x) + O(h^2)$  leading to  $h = -\frac{f(x)}{f'(x)} + O(h^2)$ . Throughout the algorithm we will test if  $f(x) < tol$ , if that is not the case we update solution  $x$  as

$x^{n+1} = x^n + h = x^n - \frac{f(x^n)}{f'(x^n)}$ , with an error of  $O(h^2)$ . The above steps can be expanded to multivariate systems as  $\mathbf{x}^{n+1} = \mathbf{x}^n - J^{-1} \vec{f}(\mathbf{x}^n)$  where  $\mathbf{x} = [x_1, \dots, x_m]^T$  and  $\vec{f}(\mathbf{x}) = [f_1(\mathbf{x}), \dots, f_n(\mathbf{x})]^T$  and  $J$  is the Jacobian defined as:

$$J = \nabla_{\mathbf{x}} \vec{f} = \begin{bmatrix} \frac{\partial f_1(\mathbf{x})}{\partial x_1} & \cdots & \frac{\partial f_1(\mathbf{x})}{\partial x_m} \\ \vdots & \ddots & \vdots \\ \frac{\partial f_n(\mathbf{x})}{\partial x_1} & \cdots & \frac{\partial f_n(\mathbf{x})}{\partial x_m} \end{bmatrix}$$

Since it is needed to solve for more variables simultaneously  $(\vec{v}^h, p^h)$ , the system must be concatenated as follows:

$$R^h = \begin{bmatrix} R_1^h(\vec{v}_h, \vec{w}_h, p_h) \\ R_2^h(\vec{v}_h, g_h) \end{bmatrix} \quad \mathbf{J} = \begin{bmatrix} \nabla_{\vec{v}^h} R_1^h(\vec{v}_h, \vec{w}_h, p_h) & \nabla_{p^h} R_1^h(\vec{v}_h, \vec{w}_h, p_h) \\ \nabla_{\vec{v}^h} R_2^h(\vec{v}_h, g_h) & \nabla_{p^h} R_2^h(\vec{v}_h, g_h) \end{bmatrix}$$

$$\begin{bmatrix} \vec{v}_{n+1}^h \\ p_{n+1}^h \end{bmatrix} = \begin{bmatrix} \vec{v}_n^h \\ p_n^h \end{bmatrix} - \mathbf{J}^{-1} \begin{bmatrix} R_1^h(\vec{v}_h, \vec{w}_h, p_h) \\ R_2^h(\vec{v}_h, g_h) \end{bmatrix} \quad (16)$$

where  $\vec{v}^h$  entries are interlaced as  $\vec{v}^h = [v_{11}^h, v_{12}^h, \dots, v_{n1}^h, v_{n2}^h]^T$ . Recalling that the system is linear respect to the test functions  $\vec{w}^h = \sum_j^K w_i^j \mathbf{e}_j \hat{\phi}_i(x_1, x_2)$  and  $g^h = \sum_i^M g_i \hat{\psi}_i(x_1, x_2)$  we can simplify coefficients  $w_j^i$  and  $g_i$  from the residual formulations as  $R_1^h(\vec{v}_h, \hat{\phi}, p_h)$  and  $R_2^h(\vec{v}_h, \hat{\psi})$ . The partial derivatives in each entry of the Jacobian matrix will then be evaluated using central differences as:

$$\begin{cases} \nabla_{\vec{v}^h} R_1^h(\vec{v}_n^h, \hat{\phi}, p_n^h)_{ij} = \frac{R_1^h(\vec{v}_n^h + \epsilon \hat{\phi}_j, \hat{\phi}_i, p_n^h) - R_1^h(\vec{v}_n^h - \epsilon \hat{\phi}_j, \hat{\phi}_i, p_n^h)}{2\epsilon} \\ \nabla_{p^h} R_1^h(\vec{v}_n^h, \hat{\phi}, p_n^h)_{ij} = \frac{R_1^h(\vec{v}_n^h, \hat{\phi}_i, p_n^h + \epsilon \hat{\psi}_j) - R_1^h(\vec{v}_n^h, \hat{\phi}_i, p_n^h - \epsilon \hat{\psi}_j)}{2\epsilon} \\ \nabla_{\vec{v}_n^h} R_2^h(\vec{v}_n^h, \hat{\psi})_{ij} = \frac{R_2^h(\vec{v}_n^h + \epsilon \hat{\phi}_j, \hat{\psi}_i) - R_2^h(\vec{v}_n^h - \epsilon \hat{\phi}_j, \hat{\psi}_i)}{2\epsilon} \\ \nabla_{p_n^h} R_2^h(\vec{v}_n^h, \hat{\psi})_{ij} = 0 \end{cases} \quad (17)$$

Note that  $R_2^h(\vec{v}_n^h, \hat{\psi})$  is independent of  $p^h$ , leading the bottom right block of the Jacobian to be zero everywhere. The above equations will be evaluated at each iteration of Newton-Raphson, this means that integrals contained in eq.14 must be solved numerically, through *Gaussian quadrature* as explained in sec.3.1. This routine is most efficiently carried out iteratively mapping each local element to the master element and integrating (eq.2).

## 4 Materials and Experiments

All experiment were conducted using MATLAB (version: *R2017 – b*). The four meshes depicted in fig.1 were given by the department of Biomedical Engineering and Imaging Sciences, King's College London.

### 4.1 Iteratively Dampen Boundary Conditions

Aiming at increasing the stability of Newton-Raphson, a second loop to decreasingly dampen boundary conditions as we move closer to the true solution was added, see fig. 4. It is believed that this approach will lead to a more stable convergence.

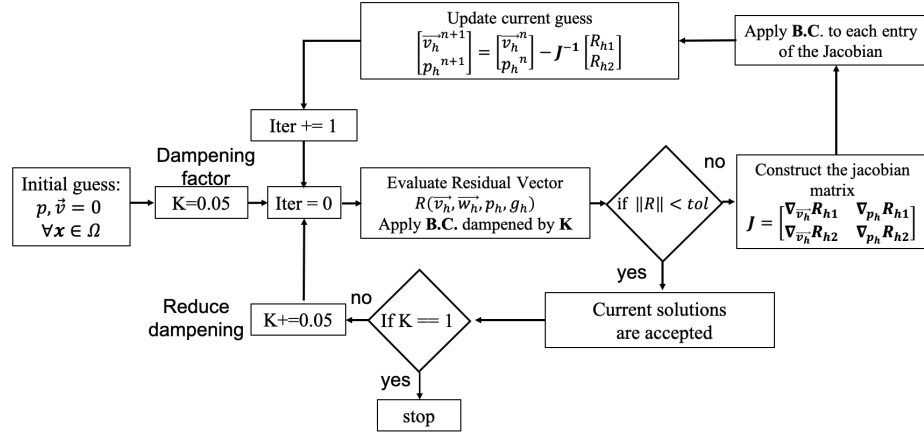


Fig. 4: Diagram depicting the modified Newton-Raphson Algorithm. Boundary conditions will be multiplied by a scalar factor  $K$  ranging from 0.05 to 1 with a step of 0.05. For each value of  $K$  Newton-Raphson will be performed to find optimal solution, which will be used as initial guesses for the next  $K$  value, at  $K = 1$  the algorithm will stop.

### 4.2 Pressure Drop Evaluation

Once the velocity and pressure fields are found, focus will be put to evaluate the pressure drop between the inlet and outlet boundaries and will be compared to results of [14]. This will be done evaluating the difference between the mean inlet pressure and the mean outlet pressure. Such means will be evaluated using two approaches:

1. *Assuming regular mesh*: under the assumption of a regular mesh one can evaluate the mean pressure simply as the algebraic mean of the pressure values on a boundary.
2. *Allowing for an adaptive mesh*: if the distance between consecutive nodes on a given boundary is not constant, one should evaluate the mean pressure as the integral of the pressure along that boundary divided by boundary length. We chose to use trapezium rule integration, but any numerical integration algorithm which allows for irregular steps can be used.

## 5 Results

The method did not converge if not iteratively damped as explained in sec.4.1, the following results were all obtained through the modified version of Newton-Raphson.

Fig.5 reports the surface plot of the  $x_1$  component of the velocity field for each mesh used.

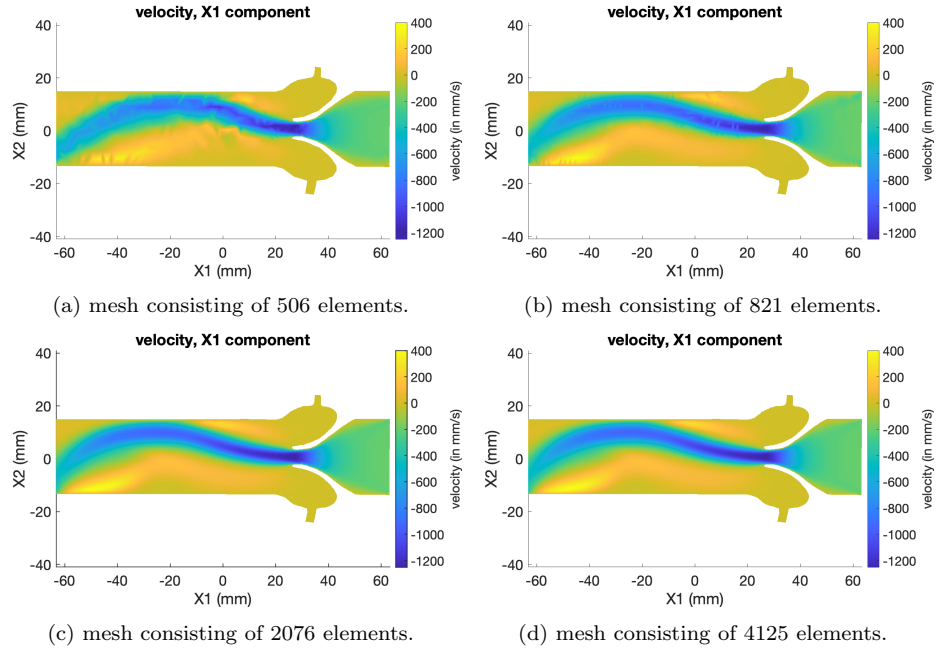


Fig. 5: Diagram depicting the  $x_1$  component of the velocity field for each mesh used. The vertical and horizontal axis respectively represent the  $x_2$  and  $x_1$  coordinates of the domain  $\Omega$ , the value of the velocity is color-coded according to the reported color-bars. All figures present the same color-bar limits of  $[-1250\text{mm/s}, 400\text{mm/s}]$  to allow comparison.

Fig.6 reports the surface plot of the  $x_1$  component of the velocity field for each mesh used.

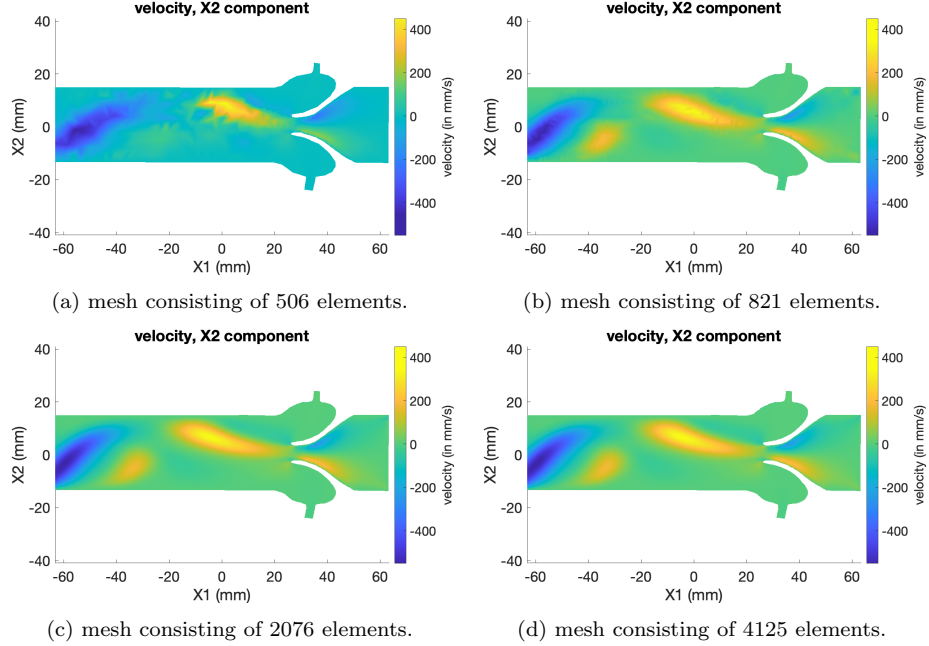


Fig. 6: Diagram depicting the  $x_2$  component of the velocity field for each mesh used. The vertical and horizontal axis respectively represent the  $x_2$  and  $x_1$  coordinates of the domain  $\Omega$ , the value of the velocity is color-coded according to the reported color-bars. All figures present the same color-bar limits of  $[-550\text{mm/s}, 450\text{mm/s}]$  to allow comparison.

Tab.1 reports the calculated pressure drops and the convergence time needed to solve the problem for each mesh used.

Table 1: Table reporting the results of the pressure drop and timing experiments explained in sec.4.2 for each of the four meshes used. Note how the computational time exponentially increases as the mesh becomes more and more refined

Mesh Density	Mean Pressure Drop			Comp. Time
	Algebraic Mean	Trapezium Rule	% difference	
506 nodes	527.686 Pa	531.153 Pa	$\approx 0.7\%$	10 min 37 sec
821 nodes	639.329 Pa	637.258 Pa	$\approx -0.3\%$	21 min 11 sec
2076 nodes	625.438 Pa	624.084 Pa	$\approx -0.2\%$	63 min 53 sec
4125 nodes	641.936 Pa	638.084 Pa	$\approx -0.6\%$	179 min 12 sec

Fig.7 reports the surface plot of the pressure field for each mesh used.

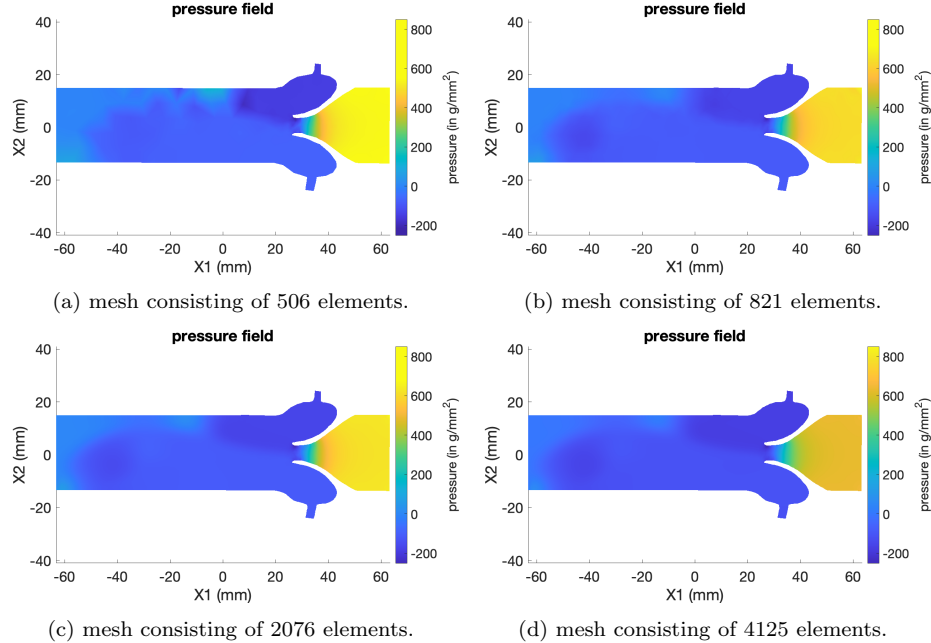


Fig. 7: Diagram depicting the pressure field for each mesh used. The vertical and horizontal axis respectively represent the  $x_2$  and  $x_1$  coordinates of the domain  $\Omega$ , the value of the pressure is color-coded according to the reported color-bars. All figures present the same color-bar limits of  $[-250Pa, 850Pa]$  to allow comparison.

## 6 Discussion

Results shown in figs.5,6 and 7 respectively show the  $x_1$ ,  $x_2$  components of the velocity field and the scalar pressure field through the domain  $\Omega$ . We can see that for the simplest mesh each solution presents discontinuities which iteratively disappear as the mesh gets refined. This gives some confidence that the error reduces as the mesh gets more accurate. Regarding convergence stability, we can see that results do not vary greatly between the two most refined meshes, this can be seen as an indicator of accuracy. On the other hand we can clearly see that between meshes 1 and 4 each variable vary greatly, indicating that the simplest meshes are not accurate enough. Note that on top of errors stemming from the mesh refinement or the finite approximation of the true solution, an error of the order of  $O(h^2)$  arises from the very nature of Newton-Raphson Algorithm (explained in sec.3.4) that we cannot recover refining the mesh.

Figs.5,6 show an interesting pattern for both velocity components, it is assumed that such patterns derive from the given boundary conditions and future work should

focus in trying different inflow boundary conditions to then analyse the results. A first approach to this end can be found in Appendix A, where the velocity distributions at different dampening values  $K$  are shown. We can see that the velocity distributions are highly affected by the given boundary values, these observations may be extrapolated to optimize the design of artificial leaflets like it was done by [14], described in sec.2. However, recall that numerous assumptions were taken throughout the problem, indicating that more investigation than a mere uniform inflow are needed for a full understanding of the phenomenon.

Results on the pressure drop show that both methods proposed in sec.4.2 gave fairly similar results, confirming our initial hypothesis that even if the meshes adaptively refine on areas of interest, they are rather homogeneous on the boundaries, as the % difference between the two methods is always  $< 1\%$ . Evaluating some statistics on the pressure drop values reported in tab.1, we find that assuming an homogeneous mesh gives an average pressure drop of  $608.5972Pa \pm 54.4247Pa$  whereas dropping that assumption gives an average pressure drop of  $607.6449Pa \pm 51.3963Pa$ . Integrating using trapezium rule gave lower variance throughout the meshes, confirming the assumption of it being the most reliable method to evaluate the pressure drop among the two proposed. Note that discarding the simplest mesh from the statistical analysis, which was observed to yield inaccurate results, the variance between the pressure drops evaluations significantly drops to  $635.568Pa \pm 8.869Pa$  and  $633.142Pa \pm 7.855Pa$  respectively for methods 4.2(1) and 4.2(2). These observations, coupled with the “visual assessment” of convergence analysis<sup>2</sup>, strengthen the assumption that the simulation was accurate for the most refined meshes. Furthermore, a visualization of the pressure drops can be seen in fig.7, which depicts larger pressure values (yellow) in the inlet respect to the outlet (blue), confirming again the assumptions. Note that this does not mean that the total error  $\epsilon$  is low, as generally  $\epsilon = \epsilon_{modelling} + \epsilon_{simulation}$  [22]. The above observations indicated a low  $\epsilon_{simulation}$ , but due to the large number of assumptions taken it is likely that  $\epsilon_{modelling}$  is rather large.

Finally, comparing the achieved pressure drops reported in tab.1 to the results achieved by [14] (recall:  $p_{drop} = [0.02 \text{ KPa}, 0.185 \text{ KPa}]$  for Reynold numbers in [10, 2000]) we can see that our results show significantly higher pressure drops, note that we did not use laminar flow and therefore the comparison is not strict, but shows that clearly something is wrong with the results, perhaps we used too many assumptions. All previous observations indicate the simulation went through successfully, leading to the conclusions that errors are mainly due to the over-simplified modelling of the problem. To this end future work should include dropping as much of those assumptions as possible, perhaps considering a pulsatile flow to emulate the heart beat, giving insights to the velocity and pressure distributions over cyclic-time and considering the aorta walls as a hyper-elastic material that undergoes deformation. However, more investigation should be conducted also regarding convergence and achieved errors, perhaps introducing an a-priori and an a-posteriori error analysis that was excluded from this paper. More importantly, as previously hinted, more boundary conditions should be tested to further investigate the flow of blood within the domain under different circumstances.

---

<sup>2</sup> from FEM theory convergence analysis states that consistent results between different meshes can be interpreted as an indicator of accuracy.

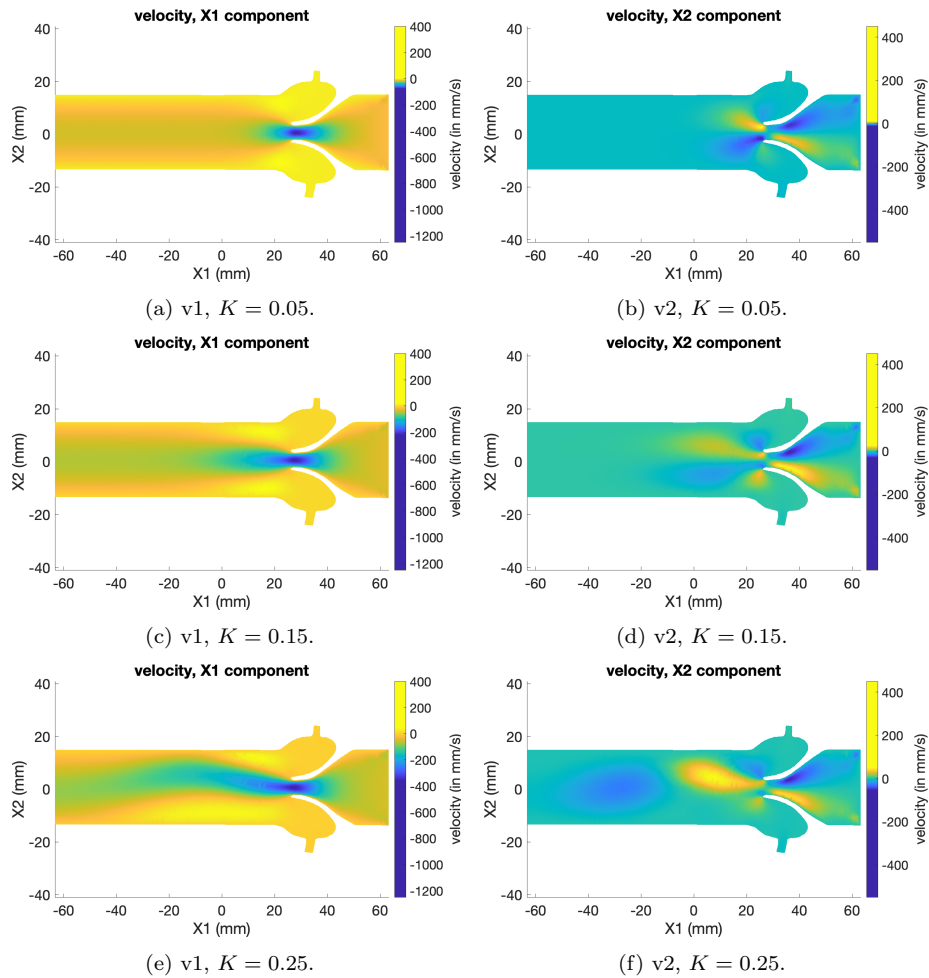
## References

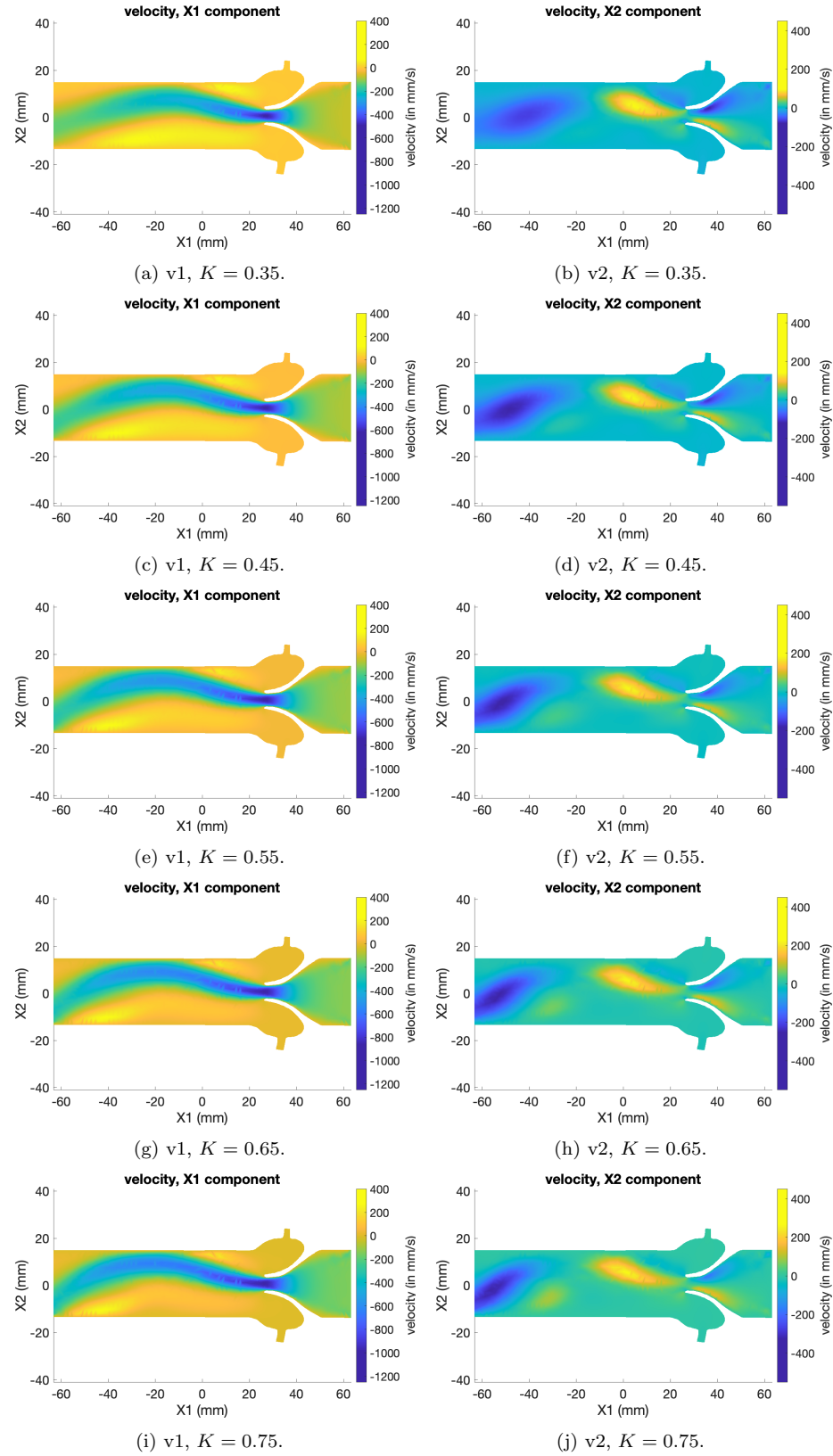
1. Carabello, B.A. and Paulus, W.J., 2009. Aortic stenosis. *The lancet*, 373(9667), pp.956-966.
2. Horstkotte, D. and Loogen, F., 1988. The natural history of aortic valve stenosis. *European heart journal*, 9(suppl-E), pp.57-64.
3. Webb, J.G., Pasupati, S., Humphries, K., Thompson, C., Altwegg, L., Moss, R., Sinhal, A., Carere, R.G., Munt, B., Ricci, D. and Ye, J., 2007. Percutaneous transarterial aortic valve replacement in selected high-risk patients with aortic stenosis. *Circulation*, 116(7), pp.755-763.
4. Makkar, R.R., Fontana, G.P., Jilaihawi, H., Kapadia, S., Pichard, A.D., Douglas, P.S., Thourani, V.H., Bablarios, V.C., Webb, J.G., Herrmann, H.C. and Bavaria, J.E., 2012. Transcatheter aortic-valve replacement for inoperable severe aortic stenosis. *New England Journal of Medicine*, 366(18), pp.1696-1704.
5. Zoghbi, W.A., Farmer, K.L., Soto, J.G., Nelson, J.G. and Quiñones, M.A., 1986. Accurate noninvasive quantification of stenotic aortic valve area by Doppler echocardiography. *Circulation*, 73(3), pp.452-459.
6. Skjaerpe, T.E.R.J.E., Hegrenæs, L.A.R.S. and Hatle, L., 1985. Noninvasive estimation of valve area in patients with aortic stenosis by Doppler ultrasound and two-dimensional echocardiography. *Circulation*, 72(4), pp.810-818.
7. Otto, C.M., Burwash, I.G., Legget, M.E., Munt, B.I., Fujioka, M., Healy, N.L., Kraft, C.D., Miyake-Hull, C.Y. and Schwaegler, R.G., 1997. Prospective study of asymptomatic valvular aortic stenosis: clinical, echocardiographic, and exercise predictors of outcome. *Circulation*, 95(9), pp.2262-2270.
8. Beraia M, Beraia G (2018) Electromagnetic properties of the arterial blood flow. *Biol Eng Med* 2: doi: 10.15761/BEM.1000141
9. Gijsen, F.J., van de Vosse, F.N. and Janssen, J.D., 1999. The influence of the non-Newtonian properties of blood on the flow in large arteries: steady flow in a carotid bifurcation model. *Journal of biomechanics*, 32(6), pp.601-608.
10. Johnston, B.M., Johnston, P.R., Corney, S. and Kilpatrick, D., 2004. Non-Newtonian blood flow in human right coronary arteries: steady state simulations. *Journal of biomechanics*, 37(5), pp.709-720.
11. Irgens, F., 2014. Rheology and non-newtonian fluids. New York: Springer International Publishing. pp.125-141.
12. Fay, J.A., 1994. Introduction to fluid mechanics. MIT press, pp.266-272.
13. Fay, J.A., 1994. Introduction to fluid mechanics. MIT press, pp.186.
14. Idelsohn, S.R., Costa, L.E. and Ponso, R., 1985. A comparative computational study of blood flow through prosthetic heart valves using the finite element method. *Journal of biomechanics*, 18(2), pp.97-115.
15. Fay, J.A., 1994. Introduction to fluid mechanics. MIT press, pp.100-104.
16. Hughes, T.J., 2012. The finite element method: linear static and dynamic finite element analysis. Courier Corporation. pp.137.
17. Zienkiewicz, O.C., Taylor, R.L. and Zhu, J.Z., 2005. The finite element method: its basis and fundamentals. Elsevier. pp. 138-178.
18. Ganesan, S. and Tobiska, L., 2017. Finite elements: Theory and algorithms. Cambridge University Press. pp.155-159.
19. Arnold, D.N., Brezzi, F. and Fortin, M., 1984. A stable finite element for the Stokes equations. *Calcolo*, 21(4), pp.337-344.
20. Zienkiewicz, O.C., Taylor, R.L., Nithiarasu, P. and Zhu, J.Z., 1977. The finite element method (Vol. 3). London: McGraw-hill. pp 57-61.

21. Reddy, J.N., 2014. An Introduction to Nonlinear Finite Element Analysis: with applications to heat transfer, fluid mechanics, and solid mechanics. OUP Oxford. pp. 180-185,224-228.
22. Zienkiewicz, O.C., Taylor, R.L. and Zhu, J.Z., 2005. The finite element method: its basis and fundamentals. Elsevier. chapters 13-14.

## 7 Appendix A

fig.10 reports the velocity fields for different dampening factors K.





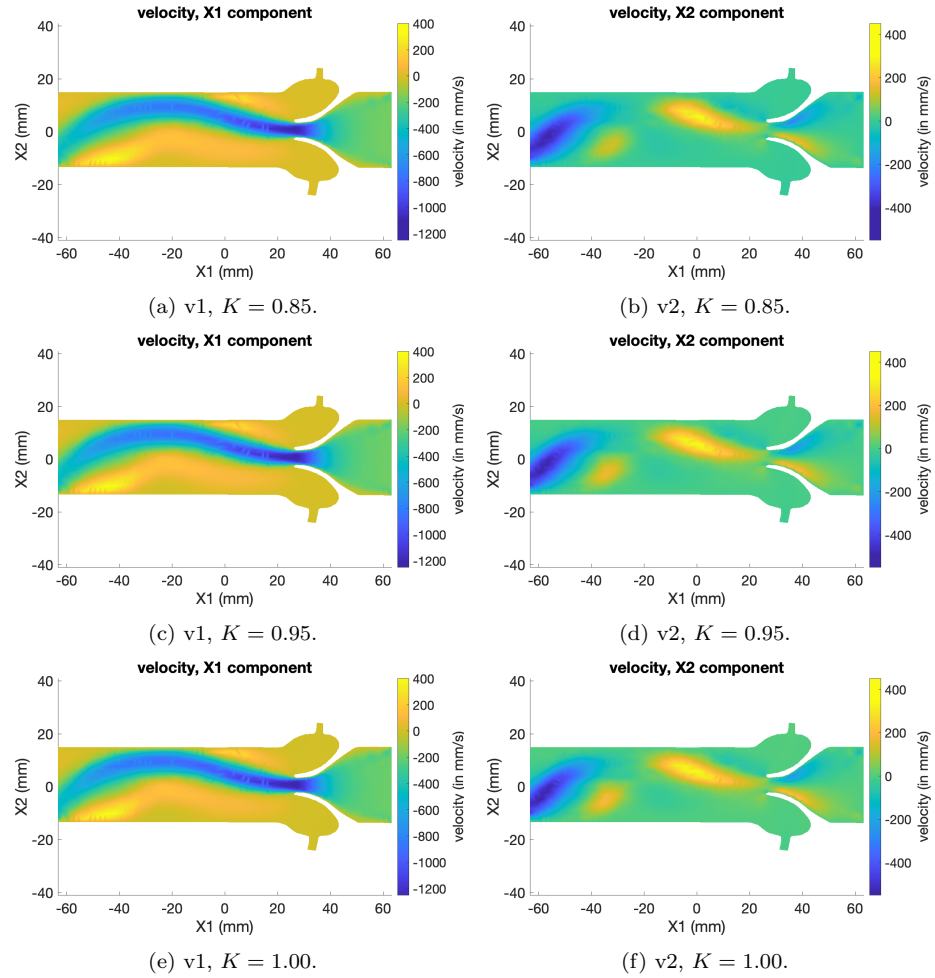


Fig. 10: Diagram depicting the velocity fields as dampening  $K$  is decreased, showing the formation of different patterns.